Research Article

Duc-Huynh Phan and Nhan Thinh Hoang*

Analysis of functionally graded porous plates using an enhanced MITC3+ element with in-plane strain correction

https://doi.org/10.1515/cls-2025-0031
received December 28, 2024; accepted June 16, 2025

Abstract: In this work, an enhanced MITC3+ approach enriched by a constant in-plane strain correction is proposed in the analysis of functionally graded (FG) porous plates. The approach involves formulating the corrected in-plane strain field through the utilization of corrected nodal derivatives in the concept of discrete divergence consistency (DDC). The DDC for the in-plane strain field is obtained through the orthogonality condition derived from the three-field variational principle (Hu-Washizu), which arises from the difference between resultant in-plane stress and in-plane strain. In carefully examining the static analysis of the FG porous plate with different elements, our investigation delves into the influence of length-to-thickness ratios, power-law indices, and porosity distributions. This comprehensive examination aims to illuminate their combined influence on the numerical outcomes. The proposed approach demonstrates superior performance in addressing FG shell problems, outperforming the original MITC3+ method.

Keywords: functionally graded porous plate, MITC3+, discrete divergence consistency, constant in-plane strain correction, first-order shear deformation theory

Nomenclature

3D	three-dimensional
CiSC	constant in-plane strain correction
CS	cell-based smoothed
DDC	discrete divergence consistency
DKMT	discrete Kirchhoff-Mindlin triangle
DKT	discrete Kirchhoff triangle
DSG3	discrete shear gap triangular
DST	discrete shear triangle
FE	finite element
FG	functionally graded
FSDT	first-order shear deformation theory
HSDT	higher-order shear deformation theory
IGA	isogeometric analysis
MITC18+	three-node triangular flat shell elements
MITC3	tensorial components for the three-node triangular element
MITC3+	effective new 3-node triangular element
MITC4	tensorial components for the four-node element

*** Corresponding author: Nhan Thinh Hoang,** Institute for Creative Design and Business, Nguyen Tat Thanh University, Ho Chi Minh City, Vietnam, e-mail: htnhan@ntt.edu.vn
Duc-Huynh Phan: Faculty of Civil Engineering, HCMC University of Technology and Education, Ho Chi Minh City, Vietnam, e-mail: huynhpd@hcmute.edu.vn

1 Introduction

In the 1980s, Japanese scholars introduced a ground breaking material known as functionally graded (FG) materials to address the heat-safeguarding challenges faced by spacecraft engines. FG materials are a special composition comprising multiple distinct phases, offering exceptional mechanical properties and high-temperature resistance. As a result, it has found extensive utilization not only in the development of heat-resistant materials but also in various fields such as electronics, chemistry, construction, and mechanical engineering. Considering the numerous benefits and wide-ranging applications mentioned above, researchers have conducted studies to study the FG structural behavior in static bending, free vibration, and buckling problems.

Due to the remarkable characteristics of FG material, a great number of researchers have proposed numerical methods to model and investigate its behavior. Bakoura *et al.* [1] pioneered the exploration of mechanical buckling in simply supported FG plates, employing a higher shear deformation theory (HSDT) in conjunction with the stress function method. Thai *et al.* [2] introduced an isogeometric

approach that employs the nonlocal strain gradient theory, grounded in the HSDT, to address challenges in solving both free vibration and static problems of FG plates. Mudhaffar *et al.* [3] provided analytical solutions using a straightforward higher-order integral shear deformation theory. Their study delves into probing the bending behavior of an FG plate subjected to hygro-thermo-mechanical loading while resting on a viscoelastic foundation. Shinde *et al.* [4] proposed a new higher-order shear and normal deformation theory to analyze the static behavior of simply supported FG shallow shells. Turan and Adiyaman [5] presented a new higher-order finite element (FE) based on parabolic shear deformation theory for the static analysis of two-directional FG porous beams subjected to various boundary conditions. Kumar *et al.* [6] gave a new inverse hyperbolic-order shear deformation theory to solve the buckling and free vibration response of porous FG plate on the foundation. Tornabene *et al.* [7] investigated the vibrational response of FG doubly-curved shell structures reinforced with carbon nanotubes short fibers using generalized differential quadrature and HSDT. Zaitoun *et al.* [8] introduced an effective method employing the HSDT with four unknowns to elucidate the buckling behavior of the FG sandwich plates positioned on a viscoelastic medium within a hygrothermal environment. Civalek *et al.* [9] studied the buckling analysis of restrained nanobeam with FG material *via* nonlocal Euler–Bernoulli beam theory using the Fourier series. Gupta and Talha [10] investigated the static and stability behavior of a geometrically imperfect FG plate with microstructural porosity on a Pasternak elastic foundation. Malekzadeh and Shojaee [11] used unified formulation and new four-variable first-order shear deformation theory (FSDT) and HSDT for the free vibration analysis of FG plates. Chanda and Sahoo [12] employed the inverse hyperbolic shear deformation theory to investigate the flexural behavior of smart FG plates. Baltacıoğlu and Civalek [13] proposed numerical solution based on Love's shell theory and FSDT for the free vibration problem of FG and carbon nanotube reinforced circular cylindrical panel. Wang *et al.* [14] pioneered a mesh-free radial basis collocation method grounded in FSDT, offering insights into the static and dynamic behavior of FG shells. Brischetto and Cesare [15] developed a coupled three-dimensional (3D) exact electro-elastic shell model for vibration analysis of multilayered composite and FG piezoelectric plates and shells. Ramteke and Panda [16] proposed the higher-order displacement functions and shear stress continuity to solve the free vibrational frequencies of multi-directional FG structures. Tornabene *et al.* [17] developed the generalized differential quadrature method to investigate the modal response of laminated anisotropic doubly-curved shell structures of variable thickness made of FG material. Ghumare and Sayyad [18] introduced a novel fifth-order plate theory and applied it to assess the static response of FG plates subjected to nonlinear hygro-thermo-mechanical loading while resting on a Winkler–Pasternak elastic foundation. In a more recent development, Liu *et al.* [19] applied an isogeometric analysis approach to conduct nonlinear analyses of the FG shells.

Recently, the incorporation of porosities into FG materials (FG porous structures) marks a notable stride in the development of this material. Nevertheless, these porosities possess the capacity to substantially change the intrinsic properties of the original FG materials. Consequently, a comprehensive exploration of the influence of porosity on the mechanical behaviors of FG materials becomes imperative. Zghal *et al.* [20] contributed to this understanding by proposing a refined mixed FE beam theory, specifically tailored to analyze the impact of porosity on the static bending behavior of FG beams. Teng and Wang [21], utilizing Galerkin analytical solutions based on the von Kármán nonlinear plate theory, addressed the nonlinear dynamic challenges in graphene platelet-reinforced porous plates. For an overview, Wu *et al.* [22] presented available research works on FG porous structures and highlighted the main advances of these structures.

In the field of plate/shell analysis, triangular planar FE elements (discrete Kirchhoff triangle (DKT) [23], discrete shear triangle (DST) [24], siscrete Kirchhoff-Mindlin triangle (DKMT) [25], DSG3 [26], MITC3 [27]) are favored for their enhanced flexibility in meshing intricate and arbitrary geometries, as well as their ability to prevent free membrane locking. Nonetheless, these elements tend to demonstrate low accuracy compared to quadrilateral FE elements (MITC4 [28]). As part of the ongoing effort to establish an ideal shell element, Lee *et al.* [29] introduced an efficient triangular MITC3+ approach. The effectiveness of the MITC3+ shell element, compared to the well-known DKT, DST, DKMT, DSG3, and MITC3 elements, has been demonstrated in the studies by Lee *et al.* [29,30]. This shell element not only successfully met all fundamental tests but also showed superior solutions. To improve the MITC3+ element, Chau-Dinh [31] introduced a MITC18+ flat shell element achieved through a combination of the Allman's membrane and MITC3+ plate. In this configuration, the membrane and bending strains undergo consistent smoothing through the utilization of cell-based strain (CS) smoothing [32], referred to as CS-MITC18+. This approach is specifically designed to elevate the performance of the MITC18+ flat shell element in both static and free vibration analyses. In the quest for an optimized triangular plate/shell element, Nguyen *et al.* [33] has innovatively introduced a linear composite bending

strain MITC3+ flat shell element, named κMITC3+. In this context, a projection operator is utilized to formulate an assumed composite bending strain field, drawing upon the Hu-Washizu three-field principle and the orthogonality condition. This novel element is engineered with the aim of achieving superior performance, with a focus on promoting a more compliant bending behavior.

To consistently improve superior properties of the MITC3 elements, this study proposed a novel constant in-plane strain correction for the MITC3 plate element, named as CiSC-MITC3+, for static analysis of the FG porous plate structures. In this framework, the corrected in-plane strain field is formulated using corrected nodal derivatives, ensuring adherence to the discrete divergence consistency (DDC) [34]. In this study, the DDC concept originates from the orthogonality condition governing the differences between resultant in-plane stress and in-plane strain as defined in the Hu-Washizu three-field variational principle [34,35]. Owing to this improvement, the proposed CiSC-MITC3+ plate element demonstrates exceptional performance compared to the original MITC3+ in solving the FG porous plate structures.

2 Formulations of FG porous plates

2.1 Material properties

In this study, we examine two distinct porosity distributions of a plate made of FG materials, its dimensions denoted as length a, width b, and thickness h, as depicted in Figure 1. The evaluation of Young's modulus E, Poisson's ratio ν, and mass density ρ for the FG plate is performed by applying the rule of mixtures, as expressed in the following equation:

$$\begin{cases} E(z) = E_m + (E_c - E_m)\left(\frac{1}{2} + \frac{z}{h}\right)^{p_z} \\ \nu(z) = \nu_m + (\nu_c - \nu_m)\left(\frac{1}{2} + \frac{z}{h}\right)^{p_z} \\ \rho(z) = \rho_m + (\rho_c - \rho_m)\left(\frac{1}{2} + \frac{z}{h}\right)^{p_z}, \end{cases} \tag{1}$$

where the symbols c and m represent the volume fraction pertaining to the ceramic and metal phases, respectively; and p_z represents the power-law index describing the gradient of materials along the plate thickness directions.

FG porous plates are fabricated using various techniques, including powder metallurgy, spray pyrolysis, and spark plasma sintering. The benefits associated with FG porous plates encompass enhanced mechanical characteristics such as increased toughness, improved energy absorption, and reduced weight when compared to conventional nonporous plates. Nonetheless, the presence of porosity within FG plates can potentially diminish their mechanical characteristics, encompassing parameters such as mass density ρ, Young's modulus E, and Poisson's ratio ν. Within this investigation, we focus on examining two distinct porosity types: uniform distribution and non-uniform distribution. These two types of distributions are mathematically defined by the subsequent equations:

- Even porosity type:

$$\begin{cases} E(z) = E_m + (E_c - E_m)\left(\frac{1}{2} + \frac{z}{h}\right)^{p_z} - \frac{\xi}{2}(E_c + E_m) \\ \nu(z) = \nu_m + (\nu_c - \nu_m)\left(\frac{1}{2} + \frac{z}{h}\right)^{p_z} - \frac{\xi}{2}(\nu_c + \nu_m) \\ \rho(z) = \rho_m + (\rho_c - \rho_m)\left(\frac{1}{2} + \frac{z}{h}\right)^{p_z} - \frac{\xi}{2}(\rho_c + \rho_m). \end{cases} \tag{2}$$

- Uneven porosity type:

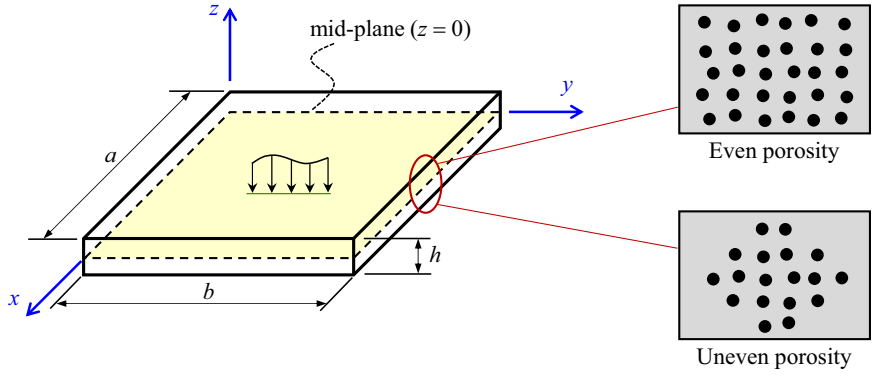

Figure 1: An FG porous plate model.

$$\begin{cases} E(x,z) = E_m + (E_c - E_m)\left(\frac{1}{2} + \frac{z}{h}\right)^{p_z} \\ \qquad - \frac{\xi}{2}\left(1 - \frac{2|z|}{h}\right)(E_c + E_m) \\ \nu(x,z) = \nu_m + (\nu_c - \nu_m)\left(\frac{1}{2} + \frac{z}{h}\right)^{p_z} \\ \qquad - \frac{\xi}{2}\left(1 - \frac{2|z|}{h}\right)(\nu_c + \nu_m) \\ \rho(x,z) = \rho_m + (\rho_c - \rho_m)\left(\frac{1}{2} + \frac{z}{h}\right)^{p_z} \\ \qquad - \frac{\xi}{2}\left(1 - \frac{2|z|}{h}\right)(\rho_c + \rho_m), \end{cases} \tag{3}$$

where ξ stands for the coefficient used for assessing the volume of porosity.

2.2 Weak forms based on the FSDT and the standard variational principle

According to FSDT [36] and the standard variational principle (one-field), the weak form for analysis of the FG porous plates is given as

$$\int_{\Omega} \delta\boldsymbol{\varepsilon}^T \boldsymbol{D}\boldsymbol{\varepsilon} \mathrm{d}\Omega + \int_{\Omega} \delta\boldsymbol{\gamma}^T \boldsymbol{D}_s\boldsymbol{\gamma} \mathrm{d}\Omega = \int_{\Omega} \delta\boldsymbol{u}^T \boldsymbol{q} \mathrm{d}\Omega, \tag{4}$$

where $\boldsymbol{u} = \boldsymbol{u}(\boldsymbol{x}) = \{u_0, v_0, w_0, \beta_x, \beta_y\}^T$ and $\boldsymbol{q} = \boldsymbol{q}(\boldsymbol{x})$ are the local deformation and the distributed load, respectively; and

$$\boldsymbol{D} = \begin{bmatrix} \boldsymbol{A} & \boldsymbol{B} \\ \boldsymbol{B} & \boldsymbol{C} \end{bmatrix}, \quad \boldsymbol{D}_s = \int_{-h/2}^{h/2} g(z) \begin{bmatrix} Q_{55} & 0 \\ 0 & Q_{44} \end{bmatrix} \mathrm{d}z, \tag{5}$$

with

$$(\boldsymbol{A}, \boldsymbol{B}, \quad \boldsymbol{C}) = \int_{-h/2}^{h/2} (1, z, \ z^2) \begin{bmatrix} Q_{11} & Q_{12} & 0 \\ Q_{21} & Q_{22} & 0 \\ 0 & 0 & Q_{66} \end{bmatrix} \mathrm{d}z, \tag{6}$$

$$\begin{aligned} &Q_{11} = Q_{22} = \frac{E(z)}{1 - \nu^2(z)}, Q_{12} = Q_{21} = \frac{\nu(z)E(z)}{1 - \nu^2(z)}, \\ &Q_{44} = Q_{55} = Q_{66} = \frac{E(z)}{2(1 + \nu(z))}. \end{aligned} \tag{7}$$

Note that the shear correction function $g(z)$ in Eq. (5) exhibits variation based on the plate thickness, wherein the stresses are free on both upper and lower surfaces. In the context of this study, the choice of the function $g(z)$ can be guided by the principles outlined in the study by Zenkour [37] as given below:

$$g(z) = \frac{5}{4} \cos\left(\frac{\pi z}{h}\right). \tag{8}$$

In Eq. (4), the FE approximations for in-plane strain $\boldsymbol{\varepsilon} = \boldsymbol{\varepsilon}(\boldsymbol{x})$ and shear strain $\boldsymbol{\gamma} = \boldsymbol{\gamma}(\boldsymbol{x})$ are expressed as follows:

$$\boldsymbol{\varepsilon} = \begin{Bmatrix} \boldsymbol{\varepsilon}_M \\ \boldsymbol{\varepsilon}_B \end{Bmatrix} = \begin{bmatrix} \boldsymbol{\Phi}_M \\ \boldsymbol{\Phi}_B \end{bmatrix} \boldsymbol{d} = \bigvee_I \left(\begin{bmatrix} \boldsymbol{\Phi}_M^I \\ \boldsymbol{\Phi}_B^I \end{bmatrix} \boldsymbol{d}^I \right) = \bigvee_I (\boldsymbol{\Phi}^I \boldsymbol{d}^I), \tag{9}$$

$$\boldsymbol{\gamma} = \boldsymbol{\Phi}_S \boldsymbol{d} = \bigvee_I (\boldsymbol{\Phi}_S^I \boldsymbol{d}^I), \tag{10}$$

where $\boldsymbol{\varepsilon}_M$ and $\boldsymbol{\varepsilon}_B$ are the membrance and bending strains, respectively; $\bigvee_I(\circ)$ serves as the assembly component operator for a matrix, while $\boldsymbol{d}^I$ represents the nodal unknown vector at Ith node; $\boldsymbol{\Phi}^I = \boldsymbol{\Phi}^I(\partial\boldsymbol{\varphi}^I)$ and $\boldsymbol{\Phi}_S^I = \boldsymbol{\Phi}_S^I(\boldsymbol{\varphi}^I, \partial\boldsymbol{\varphi}^I)$ are the nodal in-plane (membrane-bending) and shear strain-displacement matrices at Ith node, respectively; and $\boldsymbol{\varphi}^I = \boldsymbol{\varphi}^I(\boldsymbol{x})$ and $\partial\boldsymbol{\varphi}^I = \partial\boldsymbol{\varphi}^I(\boldsymbol{x})$, respectively, denote the standard nodal shape functions and their spatial derivatives at Ith node.

In our study, we employ the MITC3+ theory [29] to analyze flexural behavior. Consequently, the shear strain-displacement matrix in Eq. (10), derived from this theory, effectively alleviates shear-locking phenomena. The primary focus of our work is to improve performance of the original MITC3+ element in analysis of the FG porous plates through the introduction of a novel constant in-plane strain correction, denoted as CiSC-MITC3+, which is detailed in the next section.

3 Constant in-plane strain correction for MITC3+ plate element (CiSC-MITC3+)

Different from the standard variational principle examined in Section 2.2, the weak form of the proposed approach initiates with the Hu-Washizu three-field variational principle for an individual element Ω^e [35], emphasizing the in-plane component, as follows:

$$\begin{aligned} \delta\Pi_{HW} = &\int_{\Omega^e} \delta\tilde{\boldsymbol{\varepsilon}}^T \boldsymbol{D}\tilde{\boldsymbol{\varepsilon}} \mathrm{d}\Omega + \int_{\Omega^e} \delta\boldsymbol{\gamma}^T \boldsymbol{D}_s\boldsymbol{\gamma} \mathrm{d}\Omega - \int_{\Omega^e} \delta\boldsymbol{u}^T \boldsymbol{q} \mathrm{d}\Omega \\ &+ \delta\left[\int_{\Omega^e} \hat{\boldsymbol{\sigma}}^T (\boldsymbol{\varepsilon} - \tilde{\boldsymbol{\varepsilon}}) \mathrm{d}\Omega\right], \end{aligned} \tag{11}$$

where the displacement $\boldsymbol{u}$, assumed in-plane strain $\tilde{\boldsymbol{\varepsilon}}$, and assumed resultant in-plane stress $\hat{\boldsymbol{\sigma}}$ are independent variables.

By treating the assumed resultant in-plane stress $\hat{\boldsymbol{\sigma}}$ as orthogonal to the difference between the compatible in-plane strain $\boldsymbol{\varepsilon}$ and the assumed in-plane strain $\tilde{\boldsymbol{\varepsilon}}$, the three-field weak form (11) is simplified into a modified two-field version where the displacement $\boldsymbol{u}$ and the assumed in-plane strain $\tilde{\boldsymbol{\varepsilon}}$ become independent. Herein, the last term on the right-hand

side in Eq. (11) is removed, causing the first four terms to adopt a similar form to the classical one-field weak form (4). The only distinction lies in the replacement of the compatible in-plane strain $\boldsymbol{\varepsilon}$ with the assumed in-plane strain $\tilde{\boldsymbol{\varepsilon}}$. If the assumed in-plane strain $\tilde{\boldsymbol{\varepsilon}}$ is somehow derived from the displacement $\boldsymbol{u}$, *i.e.*, $\tilde{\boldsymbol{\varepsilon}} = \tilde{\boldsymbol{\varepsilon}}(\boldsymbol{u})$, and the condition,

$$\int_{\Omega^e} \hat{\boldsymbol{\sigma}}^T(\boldsymbol{\varepsilon} - \tilde{\boldsymbol{\varepsilon}})\mathrm{d}\Omega = 0, \tag{12}$$

is satisfied, the transformation of the three-field weak form (11) into the classical one-field weak form ensures that only the displacement $\boldsymbol{u}$ maintains its status as an independent variable [34].

In this study, we presume the subdivision of a MITC3+ element Ω^e into three sub-domains $\mathcal{T}_s$ ($n_s = 3$) to facilitate support domain integration, Figure 2. As a result, the weak form (11) is rewritten as the following form:

$$\begin{aligned}\delta\Pi_{HW} = &\sum_{s=1}^{n_s=3}\left(\int_{\mathcal{T}_s}\delta\tilde{\boldsymbol{\varepsilon}}^T\boldsymbol{D}\tilde{\boldsymbol{\varepsilon}}\mathrm{d}\mathcal{T}\right) + \int_{\Omega^e}\delta\boldsymbol{y}^T\boldsymbol{D}_s\boldsymbol{y}\mathrm{d}\Omega - \int_{\Omega^e}\delta\boldsymbol{u}^T\boldsymbol{q}\mathrm{d}\Omega \\ &+ \delta\left[\sum_{s=1}^{n_s=3}\left(\int_{\mathcal{T}_s}\hat{\boldsymbol{\sigma}}^T(\boldsymbol{\varepsilon} - \tilde{\boldsymbol{\varepsilon}})\mathrm{d}\mathcal{T}\right)\right].\end{aligned} \tag{13}$$

Note that for the fulfillment of the orthogonality condition (12) across the entire domain, it is imperative for this equation to be satisfied within each individual sub-domain $\mathcal{T}_s$

$$\int_{\mathcal{T}_s}\hat{\boldsymbol{\sigma}}^T(\boldsymbol{\varepsilon} - \tilde{\boldsymbol{\varepsilon}})\mathrm{d}\mathcal{T} = 0. \tag{14}$$

The central concern at present revolves around meeting the requirements of Eq. (14) through the creation of an assumed in-plane strain $\tilde{\boldsymbol{\varepsilon}}$ derived from the displacement $\boldsymbol{u}$. Our methodology entails constructing $\tilde{\boldsymbol{\varepsilon}}$ in a manner similar to Eq. (9), with a key modification involving the substitution of standard derivatives with corrected ones. Subsequently, we determine these values by satisfying the orthogonality condition (14). Based on the FE approximation for the compatible in-plane strain $\boldsymbol{\varepsilon}$ Eq. (9), a natural progression involves estimating the assumed in-plane strain $\tilde{\boldsymbol{\varepsilon}}$ (or *corrected in-plane strain*) as follows:

$$\tilde{\boldsymbol{\varepsilon}} = \bigvee_I(\tilde{\boldsymbol{\Phi}}^I\boldsymbol{d}^I), \tag{15}$$

where $\tilde{\boldsymbol{\Phi}}^I = \tilde{\boldsymbol{\Phi}}^I(\partial\tilde{\varphi}^I)$ and $\partial\tilde{\varphi}^I$ are the corrected in-plane-strain-displacement matrix and corrected derivatives at node I, respectively. Upon substituting Eqs (9) and (15) in Eq. (14), we obtain

$$\begin{aligned}&\bigvee_I\left[\int_{\mathcal{T}_s}\hat{\boldsymbol{\sigma}}^T(\boldsymbol{\Phi}^I - \tilde{\boldsymbol{\Phi}}^I)\mathrm{d}\mathcal{T}\right]\boldsymbol{d}^I = 0 \quad \text{or} \\ &\int_{\mathcal{T}_s}\hat{\boldsymbol{\sigma}}^T(\boldsymbol{\Phi}^I - \tilde{\boldsymbol{\Phi}}^I)\mathrm{d}\mathcal{T} = \boldsymbol{0}.\end{aligned} \tag{16}$$

Substituting Eqs (9) and (15) in Eq. (16) results in

$$\int_{\mathcal{T}_s}\hat{\boldsymbol{\sigma}}^T\left(\frac{\partial\varphi^I}{\partial_j} - \frac{\partial\tilde{\varphi}^I}{\partial_j}\right)\mathrm{d}\mathcal{T} = 0, \quad \text{with} \quad (_j = x, y). \tag{17}$$

Suppose that assumed resultant in-plane stress $\hat{\boldsymbol{\sigma}}$ in Eq. (17) is approximated using pth-order complete polynomial functions $\boldsymbol{r} = \boldsymbol{r}(\boldsymbol{x})$. By utilizing integration by parts, we can reformulate the constraints in Eq. (17) as follows:

$$\int_{\mathcal{T}_s}\boldsymbol{r}^T\frac{\partial\tilde{\varphi}^I}{\partial_j}\mathrm{d}\mathcal{T} = \int_{\Gamma_s}\boldsymbol{r}^T\varphi^I n_j\mathrm{d}\Gamma - \int_{\mathcal{T}_s}\frac{\partial\boldsymbol{r}^T}{\partial_j}\varphi^I\mathrm{d}\mathcal{T}, \tag{18}$$

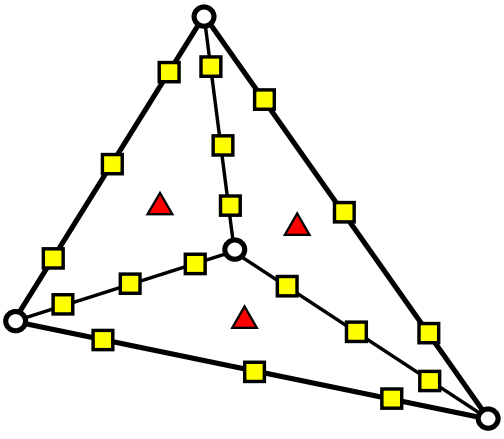

Figure 2: Numerical integration scheme in the CiSC-MITC3+ element: red triangles and yellow squares, respectively, represent the integral points for boundary and domain integrations on three sub-domains.

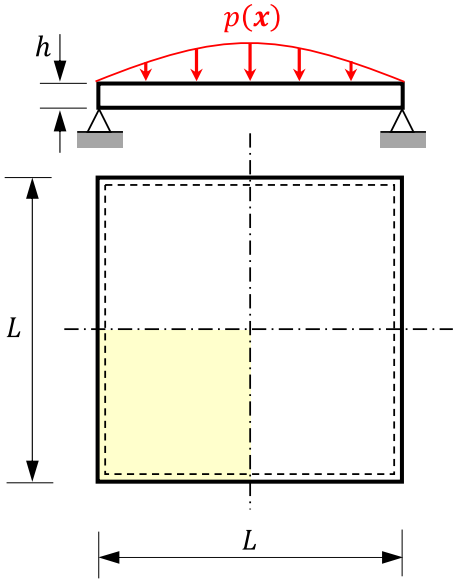

Figure 3: Isotropic plate under a sinusoidal distributed transverse load.

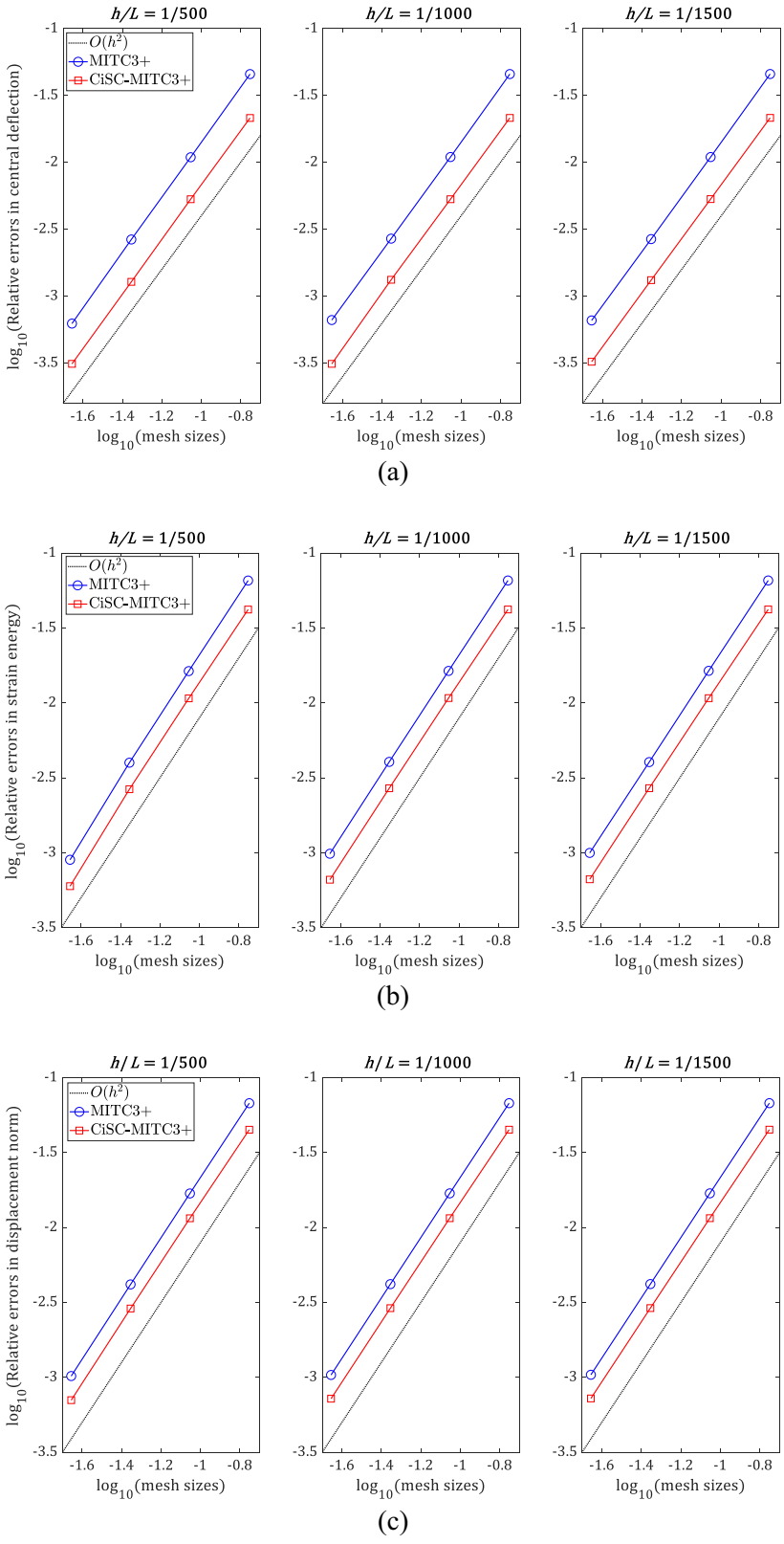

Figure 4: Convergence rates of relative errors in (a) central deflections, (b) strain energy, and (c) displacement norm for the simply supported isotropic square plate.

where n_j represents the unit normals to the boundary Γ_s of the sub-domains $\mathcal{T}_s$. It is crucial to emphasize that within the context of the divergence theorem, Eq. (18) establishes a consistency condition between nodal shape functions $\boldsymbol{\varphi}^I$ and their respective corrected derivatives $\partial\tilde{\boldsymbol{\varphi}}^I$. This fundamental relationship is termed as *divergence consistency* (DC) [34]. Through the application of numerical schemes for domain and boundary integrations, we can discretize the DC presented in Eq. (18), referred to as DDC [34], in the following manner:

$$\sum_{G=1}^{n^\Delta} \boldsymbol{r}^T(\boldsymbol{x}_G^\Delta)\frac{\partial\tilde{\varphi}^I(\boldsymbol{x}_G^\Delta)}{\partial_j}W_G^\Delta = \sum_{e=1}^{n_s=3}\sum_{g=1}^{n^\Gamma}\boldsymbol{f}^T(\boldsymbol{x}_g^e)\varphi^I(\boldsymbol{x}_g^e)W_g^e n_j^e - \sum_{G=1}^{n^\Delta}\frac{\partial\boldsymbol{r}^T(\boldsymbol{x}_G^\Delta)}{\partial_j}\varphi^I(\boldsymbol{x}_G^\Delta)W_G^\Delta, \tag{19}$$

where n^Δ and n^Γ are the number of evaluation points for domain and boundary integrations, respectively, associated with each sub-domain $\mathcal{T}_s$. In Eq. (19), the pairs $(\boldsymbol{x}_g^e, W_g^e)$ and $(\boldsymbol{x}_G^\Delta, W_G^\Delta)$ represent the integral points and their corresponding weights for boundary and domain integrations, as shown in Figure 2. These values are evaluated through a mapping from the one- and two-dimensional isoparametric element [38].

One question arises: How should we select the admissible space for the assumed resultant in-plane stress $\hat{\boldsymbol{\sigma}}$, as represented by the order of the basis function $\boldsymbol{r}$? In accordance with the suggestion by Duan *et al.* [34], a judicious decision is made to set it at least one order lower than the space of the displacement field. As an advancement over the 3-node triangular MITC3 element, the MITC3+ approach incorporates internal rotations corresponding to cubic bubble shape functions [29]. Consequently, the admissible space for the assumed resultant in-plane stress $\hat{\boldsymbol{\sigma}}$ can be selected from vectors spanning constant ($p = 0$), linear ($p = 1$), and quadratic ($p = 2$) basis functions. Based on our experience in numerical analysis, it is evident that the constant basis function consistently offers the most robust performance. In the case of the constant basis vectors, $\boldsymbol{r}(\boldsymbol{x}) = \{1\}$, the 1-point in two-dimensional triangular Gaussian quadrature rule ($n^\Delta = 1$) is applied for the domain integration in Eq. (19) due to the count of independent components. Meanwhile, the 3-point in one-dimensional Gaussian quadrature rule ($n^\Gamma = 3$) is applied for the boundary integration in Eq. (19) due to the cubic bubble approximation at the internal node. As a result, the DDC (19) is simplified into

$$\partial\tilde{\boldsymbol{\varphi}}^I(\boldsymbol{x}_C^\Delta) : \frac{\partial\tilde{\varphi}^I(\boldsymbol{x}_C^\Delta)}{\partial_j} = \frac{1}{A_C^\Delta}\sum_{e=1}^{n_s=3}\sum_{g=1}^{n^\Gamma=3}\varphi^I(\boldsymbol{x}_g^e)W_g^e n_j^e, \tag{20}$$

where A_C^Δ and $\boldsymbol{x}_C^\Delta$ denote the area and center of the sub-domain $\mathcal{T}_s$, respectively. Finally, based on the obtained correct derivatives $\partial\tilde{\boldsymbol{\varphi}}^I$ in Eq. (20), the proposed constant in-plane strain correction $\tilde{\boldsymbol{\varepsilon}}$ of MITC3+ element, named CiSC-MITC3+, is constructed within Eq. (15).

4 Results and discussion

4.1 Isotropic plate

First, we examine the convergence properties of the proposed CiSC-MITC3+ plate element in comparison to the original MITC3+ plate elements. The analysis focuses on a simply supported isotropic plate ($p_z = 0, \xi = 0$) subjected to a distributed load [39], as shown in Figure 3. This load is defined by

$$q_z(\boldsymbol{x}) = q_0 \sin\frac{\pi x}{L}\sin\frac{\pi y}{L}, \tag{21}$$

where $q_0 = 10^{-3}$ is chosen. The material properties of this isotropic square plate are: Young's modulus $E = 1{,}092{,}000$ and Poisson's ratio $\nu = 0.3$. Given the symmetric nature of the square plate, a quarter-domain is meshed into four levels (4 × 4, 8 × 8, 16 × 16, and 32 × 32).

Figure 4 presents the convergence of the relative errors in the central deflection, strain energy, and displacement norm with various thickness-and-length ratios (h/L = 1/500, 1/1,000, and 1/1,500). The displacement norm is defined in Nguyen *et al.* [40,41]. The results shown in Figure 4 highlight the uniform rates of the convergence of the proposed CiSC-MITC3+ element. These results exhibit significant enhancements of the proposed method in bending performance.

4.2 FG plates without porosity

Next the analysis of the FG nonporous square plates is examined in this example ($p_z \neq 0, \xi = 0$). Comprising a

Table 1: Mechanical properties of materials

Material	E (GPa)	ρ (kg/m^3)	ν
Metal-aluminum (Al)	70	2,700	0.3
Ceramic-alumina (Al_2O_3)	380	3,800	0.3

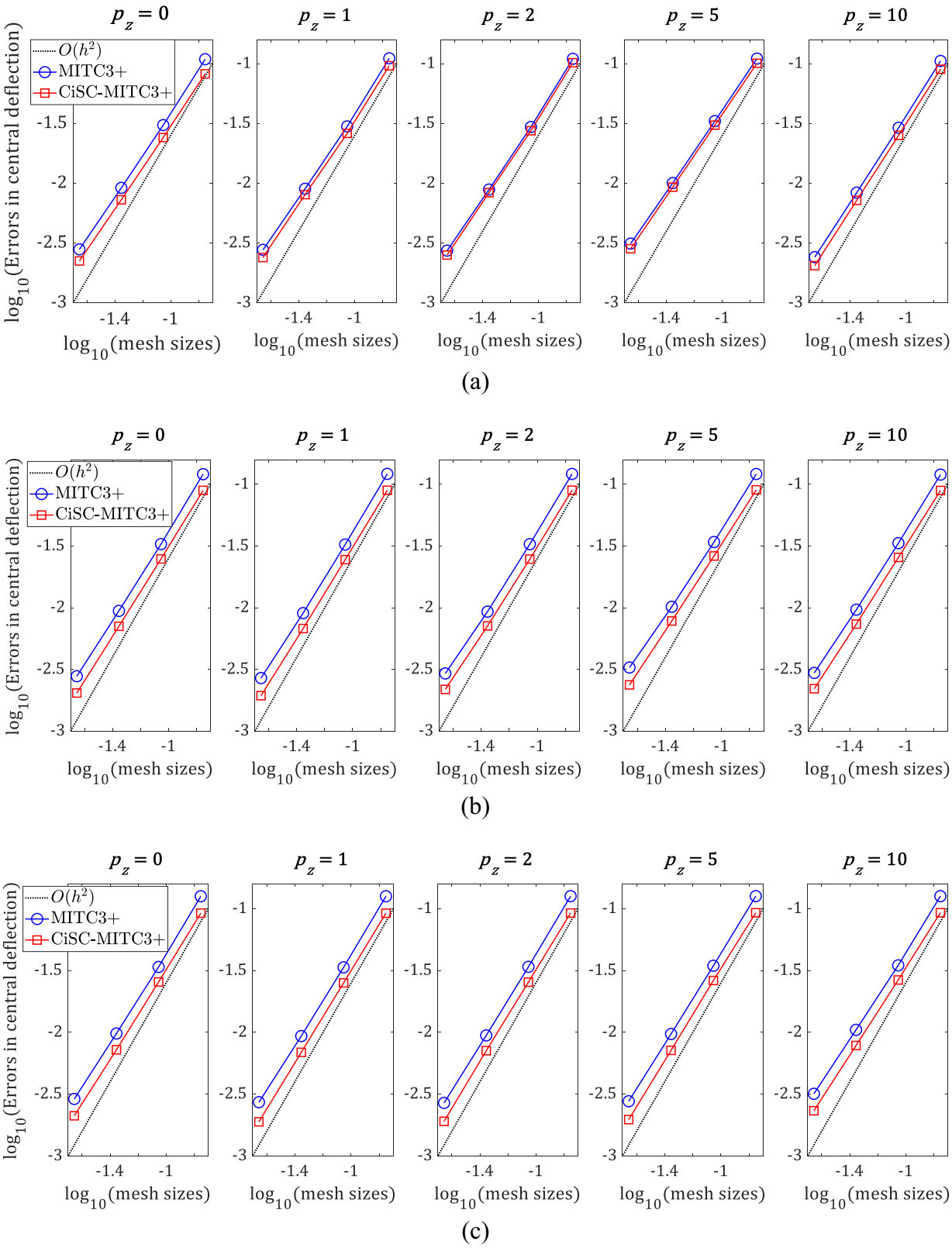

Figure 5: Comparison of the dimensionless displacement results of the nonporous FG plate with thickness-to-length ratio: (a) L/h = 5, L/h = 10, and L/h = 20.

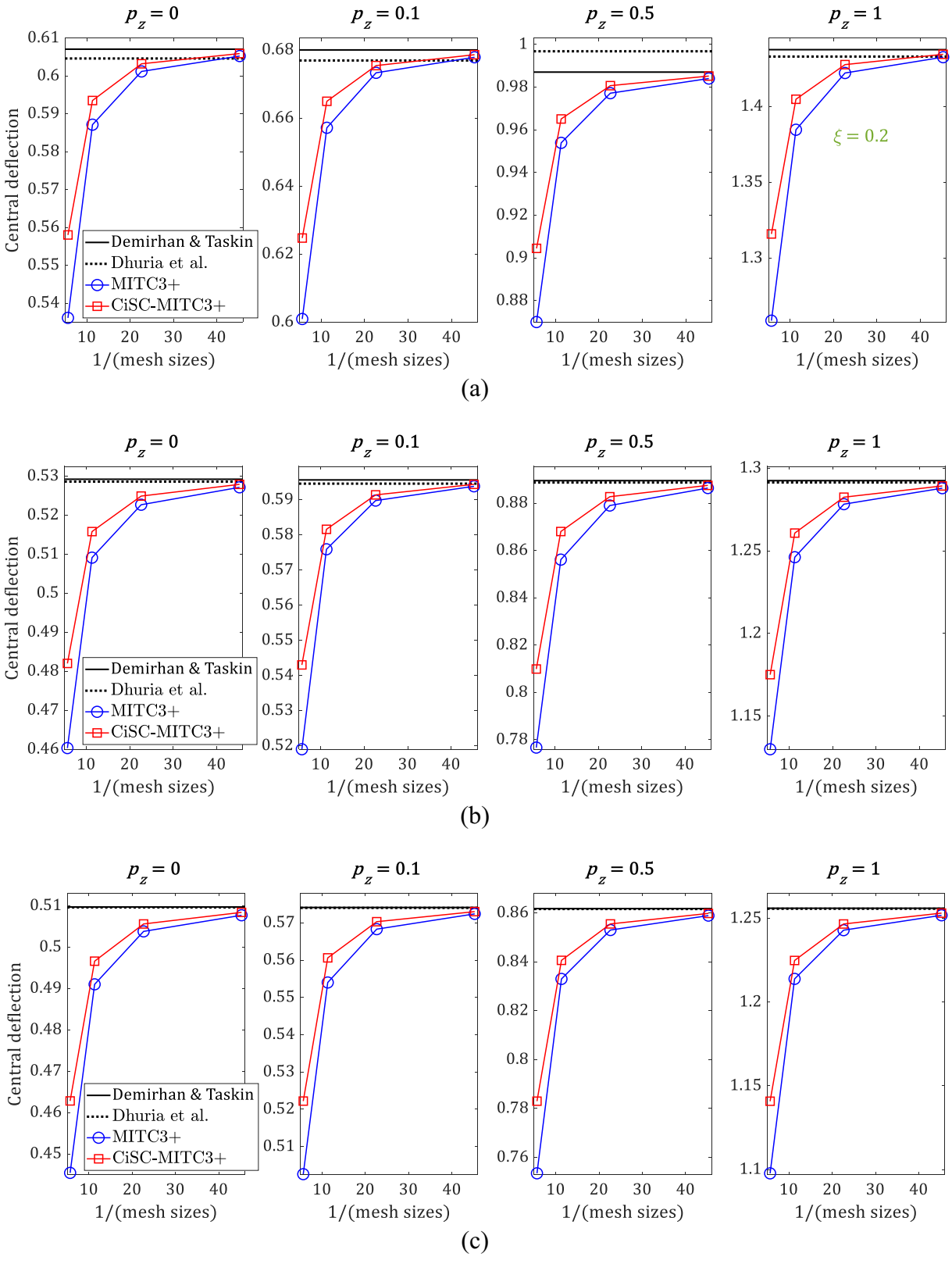

Figure 6: Convergence rates of the non-dimensional central deflections of porous FG plates with even porosity distribution across various plate length-to-thickness ratios: (a) L/h = 5, (b) L/h = 10, and (c) L/h = 20.

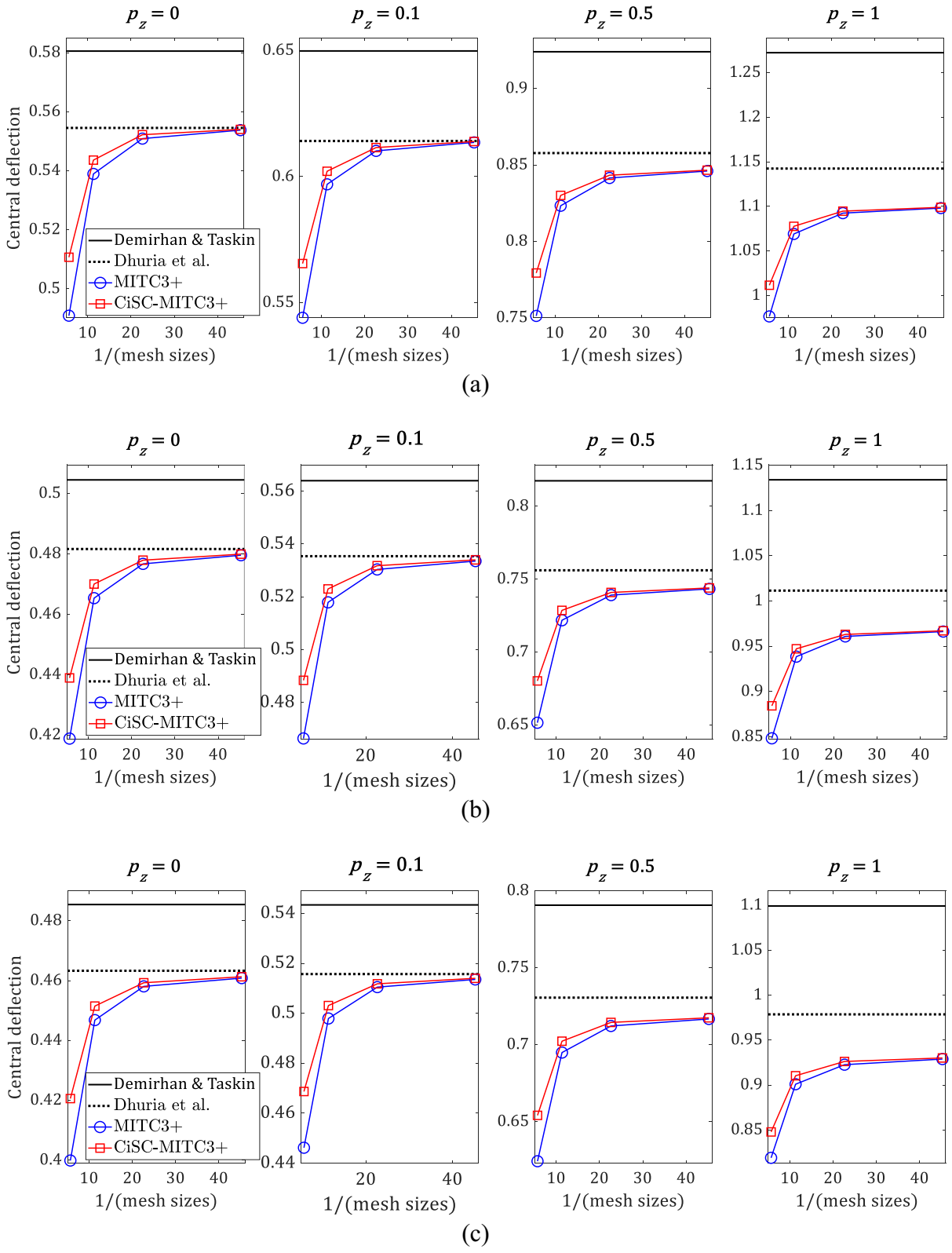

Figure 7: Convergence rates of the non-dimensional central deflections of porous FG plates with uneven porosity distribution across various plate length-to-thickness ratios: (a) L/h = 5, (b) L/h = 10, and (c) L/h = 20.

mixture of metal and ceramic (Al/Al_2O_3) as detailed in Table 1, the plate undergoes a uniform distributed load $q_0 = 1$. In this example, a quarter-domain of the square plate model is also used and discretized as in Example 3.1. For this example, the analytical Levy-type solutions are proposed by Demirhan and Taskin [42]. For the purpose of comparison, the following non-dimensional central deflection is used:

$$w^* = w\left(\frac{a}{2}, \frac{b}{2}\right). \frac{10E_c h^3}{q_0 a^4}. \tag{22}$$

The convergence rates of relative errors in the central deflection with various power-law index along thickness direction (p_z= 0, 1, 2, 5, and 10) and plate length-to-thickness ratios (L/h = 5, 10, and 20) are plotted in Figure 5. These results reconfirm the superiority of the proposed CiSC-MITC3+ elements over the original MITC3+ element.

4.3 FG porous plate

In the final example, we assess the results of the static analysis of FG porous square plates ($p_z \neq 0, \xi \neq 0$). The examined porosity distributions include both even and uneven configurations. The non-dimensional central deflection is expressed in Eq. (22). In establishing solutions for this problem, Demirhan and Taskin [42] utilized an analytical method based on a Lévy-type solution, while Dhuria *et al.* [43] employed an analytical approach following Navier's method.

Figures 6 and 7 illustrate the convergence rates of the non-dimensional central deflections of porous FG plates across various plate length-to-thickness ratios (L/h = 5, 10, and 20), power law indices (p_z = 0, 0.1, 0.5, and 1), and porosity distributions. In our investigation, we focus on a medium porosity parameter (ξ = 0.2). The results depicted in these figures demonstrate that the proposed approach aligns well with existing works. Specifically, for an even porosity distribution, our findings closely parallel those presented by Demirhan and Taskin [42]. Simultaneously, our method's results closely match the findings of Dhuria *et al.* [43] for an uneven porosity distribution. Notably, the results underscore that CiSC-MITC3+ elements consistently outperform the original MITC3+ element in both cases of porosity distributions.

5 Conclusion

This study introduces an enhancement to the MITC3+ flat shell element, specifically designed for analyzing FG porous plates identified as CiSC-MITC3+. The enhancement involves the incorporation of a novel constant in-plane strain correction, achieved by establishing a corrected in-plane strain field using corrected nodal derivatives that ensure DDC based on the Hu-Washizu three-field variational principle. The numerical investigations conducted reveal valuable insights into the proposed approach, highlighting the following two key findings:

- The proposed method demonstrates commendable performance when juxtaposed with findings from other analytical solutions of the isotropic, FG without and, FG with porous plates.
- The CiSC-MITC3+ element exhibits superior convergence in comparison to the original MITC3+ element.

In our future pursuits, we envisage expanding the application of our method to address a wide array of challenges presented by FG porous plate/shell problems, particularly those involving different loading conditions and material properties. In addition, the proposed method can be a promising approach to extend to a range of topology optimization problems [44–51].

Funding information: The authors state no funding involved.

Author contributions: Duc-Huynh Phan: Conceptualization, Methodology, Data curation, Formal analysis, Writing – original draft preparation. Nhan Thinh Hoang: Validation, Investigation, Visualization, Writing – review and editing, Supervision.

Conflict of interest: The authors state no conflict of interest.

Data availability statement: Data will be made available on request.

References

[1] Bakoura A, Bourada F, Bousahla AA, Tounsi A, Benrahou KH, Tounsi A, et al. Buckling analysis of functionally graded plates using HSDT in conjunction with the stress function method. Comput Concr. 2021;27:73–83.

[2] Thai CH, Ferreira AJM, Phung-Van P. A nonlocal strain gradient isogeometric model for free vibration and bending analyses of functionally graded plates. Compos Struct. 2020;251:112634.

[3] Mudhaffar IM, Tounsi A, Chikh A, Al-Osta MA, Al-Zahrani MM, et al. Hygro-thermo-mechanical bending behavior of advanced functionally graded ceramic metal plate resting on a viscoelastic foundation. Structures. 2021;33:2177–89.

[4] Shinde BM, Sayyad AS, Naik NS. Assessment of a new higher-order shear and normal deformation theory for the static response of functionally graded shallow shells. Curved Layer Struct. 2024;11(1):20240014.

[5] Turan M, Adiyaman GA. New higher-order finite element for static analysis of two-directional functionally graded porous beams. Arab J Sci Eng. 2023;48:13303–21.
[6] Kumar R, Lal A, Singh BN, Singh J. Meshfree approach on buckling and free vibration analysis of porous FGM plate with proposed IHHSDT resting on the foundation. Curved Layer Struct. 2019;6:192–211.
[7] Tornabene F, Viscoti M, Dimitri R. Free vibration analysis of laminated anisotropic doubly-curved shell structures reinforced with three-phase polymer/CNT/fiber material. Eng Anal Bound Elem. 2024;164:105762.
[8] Zaitoun MW, Chikh A, Tounsi A, Al-Osta MA, Sharif A, et al. Influence of the visco-Pasternak foundation parameters on the buckling behavior of a sandwich functional graded ceramic–metal plate in a hygrothermal environment. Thin-Walled Struct. 2022;170:108549.
[9] Civalek Ö, Uzun B, Yaylı MÖ. An effective analytical method for buckling solutions of a restrained FGM nonlocal beam. Comput Appl Math. 2022;41(2):67.
[10] Gupta A, Talha M. Static and stability characteristics of geometrically imperfect FGM plates resting on Pasternak elastic foundation with microstructural defect. Arab J Sci Eng. 2018;43:4931–47.
[11] Malekzadeh P, Shojaee M. A unified formulation for free vibration of functionally graded plates. Sci Eng Compos Mater. 2018;25:109–22.
[12] Chanda A, Sahoo R. Flexural behavior of functionally graded plates with piezoelectric materials. Arab J Sci Eng. 2020;45:9227–48.
[13] Baltacıoğlu AK, Civalek Ö. Vibration analysis of circular cylindrical panels with CNT reinforced and FGM composites. Compos Struct. 2018;202:374–88.
[14] Wang L, Liu Y, Zhou Y, Yang F. Static and dynamic analysis of thin functionally graded shell with in-plane material inhomogeneity. Int J Mech Sci. 2021;193:106165.
[15] Brischetto S, Cesare D. Three-dimensional vibration analysis of multilayered composite and functionally graded piezoelectric plates and shells. Compos Struct. 2024;346:118413.
[16] Ramteke PM, Panda SK. Free vibrational behaviour of multi-directional porous functionally graded structures. Arab J Sci Eng. 2021;46:7741–56.
[17] Tornabene F, Viscoti M, Dimitri R. Effect of porosity on the modal response of doubly-curved laminated shell structures made of functionally graded materials employing higher order theories. Structures. 2024;60:105848.
[18] Ghumare SM, Sayyad AS. Nonlinear hygro-thermo-mechanical analysis of functionally graded plates using a fifth-order plate theory. Arab J Sci Eng. 2019;44:8727–45.
[19] Liu N, Ren X, Lua J. An isogeometric continuum shell element for modeling the nonlinear response of functionally graded material structures. Compos Struct. 2020;237:111893.
[20] Zghal S, Ataoui D, Dammak F. Static bending analysis of beams made of functionally graded porous materials. Mech Based Des Struct Mach. 2020;50:1012–29.
[21] Teng MW, Wang YQ. Nonlinear forced vibration of simply supported functionally graded porous nanocomposite thin plates reinforced with graphene platelets. Thin-Walled Struct. 2021;164:107799.
[22] Wu H, Yang J, Kitipornchai S. Mechanical analysis of functionally graded porous structures: a review. Int J Struct Stab Dyn. 2020;20:2041015.
[23] Batoz JL, Bathe KJ, Ho LW. A study of three-node triangular plate bending elements. Int J Numer Methods Eng. 2005;15:1771–812.
[24] Batoz JL, Lardeur P. A discrete shear triangular nine D.O.F. element for the analysis of thick to very thin plates. Int J Numer Methods Eng. 2005;28:533–60.
[25] Katili I. A new discrete Kirchhoff-Mindlin element based on Mindlin-Reissner plate theory and assumed shear strain fields—part I: An extended DKT element for thick-plate bending analysis. Int J Numer Methods Eng. 2005;36:1859–83.
[26] Kai -, Uwe Bletzinger MB. Ekkehard Ramm A unified approach for shear-locking-free triangular and rectangular shell finite elements. Comput Struct. 2000;75:321–34.
[27] Lee P-S, Bathe K-J. Development of MITC isotropic triangular shell finite elements. Comput Struct. 2004;82:945–62.
[28] Bathe KJ, Dvorkin EN. A four-node plate bending element based on Mindlin/Reissner plate theory and a mixed interpolation. Int J Numer Methods Eng. 1985;21:367–83.
[29] Lee Y, Lee P-S, Bathe K-J. The MITC3+ shell element and its performance. Comput Struct. 2014;138:12–23.
[30] Ko Y, Lee Y, Lee P-S, Bathe K-J. Performance of the MITC3+ and MITC4+ shell elements in widely-used benchmark problems. Comput Struct. 2017;193:187–206.
[31] Chau-Dinh T. Analysis of shell structures by an improved 3-node triangular flat shell element with a bubble function and cell-based strain smoothing. Thin-Walled Struct. 2023;182:110222.
[32] Liu GR, Dai KY, Nguyen TTA. Smoothed finite element method for mechanics problems. Comput Mech. 2006;39:859–77.
[33] Nguyen SH, Vu T, Pham QH, Nguyen-Thoi T. An extension of composite bending strain κMITC3+ scheme in analysis of shell structures reinforced with rib stiffeners. Thin-Walled Struct. 2024;202:112062.
[34] Duan Q, Gao X, Wang B, Li X, Zhang H, Belytschko T, et al. Consistent element-free Galerkin method. Int J Numer Methods Eng. 2014;99:79–101.
[35] Chan ASL. Variational Methods in Elasticity and Plasticity. K. Washizu. Pergamon, Oxford, 1968. 350 pp. Illustrated. 120s. Aeronaut J. 1968;72(694):889.
[36] Reddy JN. Mechanics of laminated composite plates and shells. shells: Theory and analysis. Boca Raton, FL, USA: CRC Press; 2003.
[37] Zenkour AM. Generalized shear deformation theory for bending analysis of functionally graded plates. Appl Math Model. 2006;30:67–84.
[38] Liu GR, Trung N. Smoothed finite element methods. NewYork: CRC Press: Taylor and Francis Group; 2010.
[39] Timoshenko S, Woinowsky-Krieger S. Theory of plates and shells. New York, USA: McGraw-Hill; 1959. p. 580.
[40] Nguyen SH, Nam NN, Hoang T-D, Nguyen TN, Nguyen-Thoi T. Alpha (α) assumed rotations and shear strains for spatially isotropic polygonal Reissner-Mindlin plate elements (αARS-Poly). Comput Struct. 2023;274:106900.
[41] Nguyen SH, Phan D-H. Selective element domain interpolation technique for assumed rotations and shear strains in polygonal finite element thick/thin plate analysis. Thin-Walled Struct. 2023;186:110677.
[42] Demirhan PA, Taskin V. Bending and free vibration analysis of Levy-type porous functionally graded plate using state space approach. Compos Part B: Eng. 2019;160:661–76.
[43] Dhuria M, Grover N, Goyal K. Influence of porosity distribution on static and buckling responses of porous functionally graded plates. Structures. 2021;34:1458–74.

[44] Nguyen-Hoang S, Sohn D, Kim H-G. A new polyhedral element for the analysis of hexahedral-dominant finite element models and its application to nonlinear solid mechanics problems. Comput Methods Appl Mech Eng. 2017;324:248–77.
[45] Nguyen-Xuan H, Nguyen-Hoang S, Rabczuk T, Hackl K. A polytree-based adaptive approach to limit analysis of cracked structures. Comput Methods Appl Mech Eng. 2017;313:1006–39.
[46] Nguyen SH, Kim H-G. Level set based shape optimization using trimmed hexahedral meshes. Comput Methods Appl Mech Eng. 2019;345:555–83.
[47] Nguyen SH, Kim H-G. Stress-constrained shape and topology optimization with the level set method using trimmed hexahedral meshes. Comput Methods Appl Mech Eng. 2020;366:113061.
[48] Nguyen SH, Sohn D, Kim H-G. A novel hr-adaptive mesh refinement scheme for stress-constrained shape and topology optimization using level-set-based trimmed meshes. Struct Multidiscip Optim. 2022;65(2):71.
[49] Nguyen SH, Nguyen TN, Nguyen-Thoi T. A finite element level-set method for stress-based topology optimization of plate structures. Comput Math Appl. 2022;115:26–40.
[50] Ho TNT, Nguyen SH, Le VT, Hoang T-D. Coupling design and fabrication of continuous carbon fiber-reinforced composite structures using two-material topology optimization and additive manufacturing. Int J Adv Manuf Technol. 2024;130:4277–93.
[51] Nguyen SH, Ho TNT, Lieu QX, Vu T, Nguyen-Thoi T. Enhancement of MITC3+ flat shell element using curvature corrections. Acta Mech. 2025;236:2725–40.